Simulation study of the filamentation of counter-streaming beams of the electrons and positrons in plasmas

Mark E Dieckmann, P K Shukla and Lennart Stenflo

Original Publication:

Mark E Dieckmann, P K Shukla and Lennart Stenflo, Simulation study of the filamentation of counter-streaming beams of the electrons and positrons in plasmas, 2009, PLASMA PHYSICS AND CONTROLLED FUSION, (51), 6, 065015.
http://dx.doi.org/10.1088/0741-3335/51/6/065015

Simulation study of the filamentation of counter-streaming beams of the electrons and positrons in plasmas

M E Dieckmann[1,2], P K Shukla[2,3] and L Stenflo[4]

1 Department of Science and Technology, Linköping University, SE-60174 Norrköping, Sweden
2 Institute of Theoretical Physics IV, Ruhr-University Bochum, D-44780 Bochum, Germany
3 SUPA Department of Physics, University of Strathclyde, Glasgow, Scotland, and Department of Physics, Umeå University, SE-90187 Umeå, Sweden
4 Department of Physics, Chemistry and Biology, Linköping University, SE-58183 Linköping, Sweden

E-mail: markd@tp4.rub.de

Abstract. The filamentation instability driven by two spatially uniform and counter-streaming beams of charged particles in plasmas is modelled by a particle-in-cell (PIC) simulation. Each beam consists of the electrons and positrons. The four species are equally dense and they have the same temperature. The one-dimensional simulation direction is orthogonal to the beam velocity vector. The magnetic field grows spontaneously and rearranges the particles in space, such that the distributions of the electrons of one beam and the positrons of the second beam match. The simulation demonstrates that as a result no electrostatic field is generated by the magnetic field through its magnetic pressure gradient prior to its saturation. This electrostatic field would be repulsive at the centres of the filaments and limit the maximum charge and current density. The filaments of electrons and positrons in this simulation reach higher charge and current densities than in one with no positrons. The oscillations of the magnetic field strength induced by the magnetically trapped particles result in an oscillatory magnetic pressure gradient force. The latter interplays with the statistical fluctuations in the particle density and it probably enforces a charge separation, by which electrostatic waves grow after the filamentation instability has saturated.

PACS numbers: 52.40.Mj,52.27.Ep,52.65.Rr

1. Introduction

If a plasma is initially free of any net current, but if it has a nonequilibrium particle velocity distribution, then it can support the growth of magnetic fields through the redistribution of currents in space. This has been demonstrated first by Weibel [1] for a plasma with a bi-Maxwellian electron velocity distribution. The currents are rearranged through the growing plasma waves into filaments, which are separated by electromagnetic fields [2]. This is also the case for the instability driven by counterstreaming beams of charged particles, which is commonly referred to as the beam-Weibel instability or the filamentation instability (FI) [3, 4, 5, 6].

The FI can generate strong magnetic fields in astrophysical environments such as the leptonic pulsar winds [7]. The FIs are also important for the generation of cosmological magnetic fields [8] and for inertial confinement fusion [9, 10], where laser pulses accelerate electron beams to relativistic speeds. Previous simulation studies have revealed various aspects of the growth and saturation of the FI. The FI driven by two counter-propagating beams of electrons has been examined by using particle-in-cell (PIC) and Vlasov simulations. Such studies have been performed in one spatial dimension (1D) [11, 12, 13, 14, 15], in two spatial dimensions (2D) [3, 16, 17, 18] and in 3D [19]. The effects of a guiding magnetic field on counter-streaming electron beams have also been examined [18, 20]. The simulation studies in Refs. [13, 21] have investigated the impact of the ions on the non-linear stage of the FI.

The FIs are usually triggered by the electrons. The ion filamentation is slower and often coupled through electrostatic fields to the electron filamentation. The FI involving only electrons couples to electrostatic fields during its quasi-linear growth phase. We refer to this source mechanism of electrostatic waves as the quasi-linear electrostatic instability (QEI). The electrostatic field amplitude grows in response to the QEI at twice the exponential rate of the magnetic field amplitude [12, 13, 14] and it oscillates around an equilibrium value after the FI has saturated. This equilibrium amplitude is such, that it excerts a force on the electrons that equals that of the average magnetic pressure gradient force (MPGF) [15]. This was demonstrated for the case of two counter-streaming, equally dense electron beams, for which the growth rate of the purely transverse FI is highest relative to those of the competing electrostatic two-stream instability and of the partially electromagnetic mixed mode instability [22]. The omission of wavevectors aligned with the beam velocity vector is thus most realistic.

The pulsar winds carry with them positrons [7]. The impact of the positrons on the initial growth phase of the filamentation instabilities is understood, in principle, by solving the linear dispersion relation, as it has been done for example in Refs. [23, 24, 25] for the FI and in Ref. [26] for the Weibel instability. The nonlinear evolution of instabilities driven by beams of the electrons and positrons have been modelled with PIC simulations in 2D [27, 28] and in 3D [29].

In this paper, we consider two counterstreaming plasma beams, each of which contains an identical number of positrons and electrons. The FI is modelled in a short

1D simulation box, in which only one filament pair develops, as it has been done in Refs. [12, 13, 15] for the electron beams. The non-linear saturation of the FI is not captured correctly, since we exclude the filament merging and the multi-dimensional structure of the filaments [3]. However, the filaments are not circular if the beams are warm and if they have the same density. We find spatial intervals of the filaments that are planar over several electron skin depths [17, 18, 30]. A 1D simulation can give insight into the dynamics of such planar boundaries. The 1D geometry allows us to freeze the filament pair just after the initial saturation and we can analyse the filaments in an almost time-stationary form. We can isolate a single filament pair to better understand its dynamics by omitting its collective interactions with the neighboring filaments. The restriction to one spatial dimension furthermore permits us to use a good statistical representation of the plasma phase space distribution and we can reduce the simulation noise. Accurate measurements of the fields and of the phase space distribution are thus possible. We choose initial conditions, which are identical to those in Refs. [14, 15], except for the positronic beam component that we include here. This allows us to compare directly the electromagnetic interaction of two counterpropagating electron beams with that of two counterpropagating beams of the electrons and positrons.

We summarize our key results. The symmetry between the electrons and the positrons suppresses the QEI during the quasi-linear growth phase of the FI. The magnetic trapping model [11], which does not consider an electric field, accurately describes the saturation magnetic field in the simulation. The electrostatic field driven by the QEI would repel the electrons at the centre of the filament and attract those farther away [15], thus limiting the charge density accumulation due to the FI. Its absence implies that the filament confinement is stronger, if the positrons are present; higher peak density values can be reached and the spacing between the filaments is larger. The magnetic fields should reach higher spatial gradients compared to a system of counter-propagating electron beams due to the stronger currents. We could separate the purely magnetic FI driven by counter-propagating electron-positron beams from a secondary electrostatic instability (SEI), which we show to be unrelated to the QEI. The waves the SEI drives have a broadband wavenumber spectrum. We bring forward evidence for a connection between the SEI and the spatio-temporal oscillations of the MPGF. These oscillations occur on time scales, which are comparable to the inverse plasma frequency, and on spatial scales of the order of a Debye length. The MPGF can thus interplay through these oscillations with the statistical fluctuations of the plasma, by which a charge separation can occur. We propose that this separation breaks the initial symmetry of electrons and positrons and destabilizes the filament. The power of the waves driven by the SEI, which have a frequency that is close to the plasma frequency, grows in time. Its power can be fitted as a function of time by two exponential functions, which are separated by a break in the growth rate.

The manuscript is organized as follows. Section 2 briefly describes the PIC simulation method and it discusses our initial conditions. Section 3 presents our simulation results, which are then discussed in Section 4.

2. The PIC simulation method and the initial conditions

The standard particle-in-cell (PIC) method [31] can model the processes in a collisionless kinetic plasma. It approximates the plasma phase space distribution by an ensemble of volume elements or computational particles (CPs). The ensemble properties of the CPs are an approximation to the ensemble properties of the corresponding physical plasma species. Each CP with index i of the species j can have a charge q_j and mass m_j that differ from those of the plasma species they represent, e.g. the mass m_e and the charge $-e$ of an electron. The charge-to-mass ratio must be preserved though.

The CPs follow trajectories in the simulation domain, which are determined by the electric $\mathbf{E}$ and the magnetic $\mathbf{B}$ fields. The electromagnetic fields and the global current $\mathbf{J}$ are defined on a spatial grid. The equations that are solved by the PIC code are

$$\nabla \times \mathbf{E} = -\frac{\partial \mathbf{B}}{\partial t}, \quad \nabla \times \mathbf{B} = \frac{\partial \mathbf{E}}{\partial t} + \mathbf{J}, \tag{1}$$

$$\nabla \cdot \mathbf{B} = 0, \quad \nabla \cdot \mathbf{E} = \rho, \tag{2}$$

$$\frac{d\mathbf{p}_i}{dt} = q_j \left(\mathbf{E}[\mathbf{x}_i] + \mathbf{v}_i \times \mathbf{B}[\mathbf{x}_i]\right), \quad \mathbf{p}_i = m_j \, \mathbf{v}_i \, \Gamma(\mathbf{v}_i), \quad \frac{d\mathbf{x}_i}{dt} = \mathbf{v}_i. \tag{3}$$

The electromagnetic fields are evolved in time using the Faraday law and the Ampere law (Eq. (1)). Equations (2) are typically fullfilled as constraints, or they are enforced by correction steps. The virtual particle method [32] our code is using is fullfilling Poisson's equation as a constraint and $\nabla \cdot \mathbf{B} = 0$ is solved exactly in 1D and to round-off precision in higher dimensions. The trajectories of the CPs are updated using the Eqns. (3). We refer the interested reader to the Refs. [31, 32, 33, 34, 35, 36] for a more thorough discussion of numerical PIC schemes.

Equations (1)-(3) can be scaled to physical units with the total plasma frequency $\omega_p = \left(n_t e^2/m_e \epsilon_0\right)^{1/2}$ and the skin depth $\lambda_e = c/\omega_p$, where the total particle number density $n_t = \sum_j n_j$ is summed over the four leptonic species, which are equally dense. The quantities in physical units denoted by the subscript p are obtained from the normalized ones by substituting $\mathbf{E}_p = \omega_p c m_e \mathbf{E}/e$, $\mathbf{B}_p = \omega_p m_e \mathbf{B}/e$, $\mathbf{J_p} = e c n_t \mathbf{J}$, $\rho_p = e n_t \rho$, $\mathbf{x}_p = \lambda_e \mathbf{x}$, $t_p = t/\omega_p$, $\mathbf{v}_p = \mathbf{v}c$ and $\mathbf{p}_p = m_e c \mathbf{p}$. The charge q_j, in this normalization, is 1 for the positrons and -1 for the electrons, while $m_j = 1$. We also normalize $\Omega = \omega/\omega_p$ and $\mathbf{k} = \mathbf{k}_p c/\omega_p$, where $\omega, \mathbf{k}_p$ have physical units.

Both beams in our simulation study move in opposite **z**-directions with the speed modulus $v_b = 0.3$, giving the relative beam speed $2v_b/(1+v_b^2) \approx 0.55$. This v_b is about half that used in Ref. [28]. Each of the two beams consists of one electron species and of one positron species and all four species are equally dense. Initially all beams are spatially uniform. The velocity distribution in the rest frame of each beam is a Maxwellian with the thermal speed $v_t \equiv \left(kT/m_e\right)^{1/2} = v_b/18$ in all directions. The 1D simulation box with its periodic boundary conditions is aligned with the **x**-direction. Only waves with wavevectors parallel to x can grow and we use the scalar wavenumber k. The length $L = 1.25\lambda_e$ of the simulation box is identical to that of the shortest one in Ref. [15], if we neglect the positron contribution to λ_e. The simulation box is subdivided

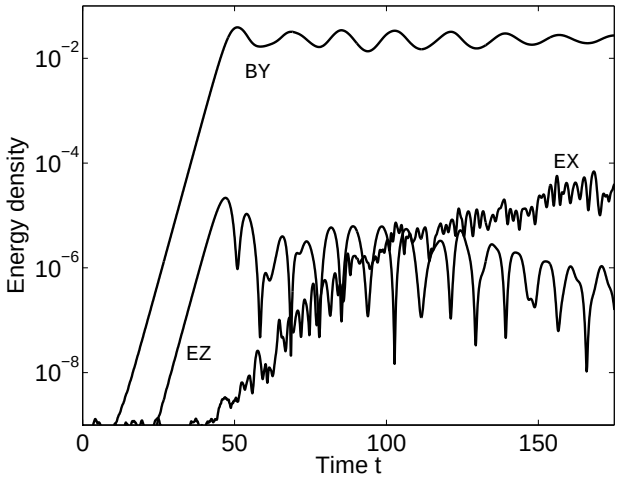

Figure 1. The energy densities in units of the total energy in the simulation: The uppermost curve E_{BY} corresponds to B_y. Its exponential rate, which is twice the Ω_i of B_y, is ≈ 0.5 during $10 < t < 50$. It oscillates around an equilibrium after that. The curves of E_{EZ} and E_{BY} grow initially at the same exponential rate, but E_{EZ} decreases for $t > 50$. The electrostatic E_{EX} starts to grow at $t \approx 45$, when E_{BY} has saturated.

into 500 grid cells of equal length Δ_x. The ratio $\Delta_x \omega_p / v_t = 0.15$ and the Debye length is resolved well. Each of the four plasma species is represented by 2.45×10^7 CPs. The $\mathbf{E} = 0$ and $\mathbf{B} = 0$ at the simulation's start. The total simulation time is $t_{sim} = 177$, which is subdivided into 10^5 time steps Δ_t.

3. Simulation results

The FI driven by a plasma flow along z and a simulation box that is aligned with x will lead to the initial growth of a magnetic field along y. The growing net current $J_z(x)$ will also result in a growing E_z by Ampere's law. An electrostatic E_x field would grow in the case of a system that is composed of two electron beams.

Figure 1 displays the energy densities of these field components, which we denote as E_{BY}, E_{EZ} and E_{EX}. The energy density E_{BY} of the magnetic B_y component dominates and it reaches a few percent of the total energy, in line with previous simulations [28]. The exponential growth rate of B_y is $\Omega_i \approx 0.25$, which is close to the expected value $\approx v_b / \gamma_b^{1/2}$ for cold beams. The E_{EZ} grows at the same rate as E_{BY}, but its values are three orders of magnitude less. The energy density E_{EX} of the electrostatic field grows after the FI has saturated. The growth rate of $E_{Ex} \propto E_x^2$ can be fitted with an exponential function with the growth rate $\Omega_{ix} \approx 0.13$ between $45 < t < 90$ and with a second, slower growing one for $t > 100$. The growth of E_{EX} in Fig. 1 can not be attributed to the QEI, because then the E_{EX} should grow at twice the exponential rate of E_{BY} until $t \approx 50$ and oscillate around an equilibrium value after that time.

We look in more detail at the fields to better understand the cause of the oscillations of E_{BY} around its equilibrium and the source mechanism of the growth of E_{EX}. The

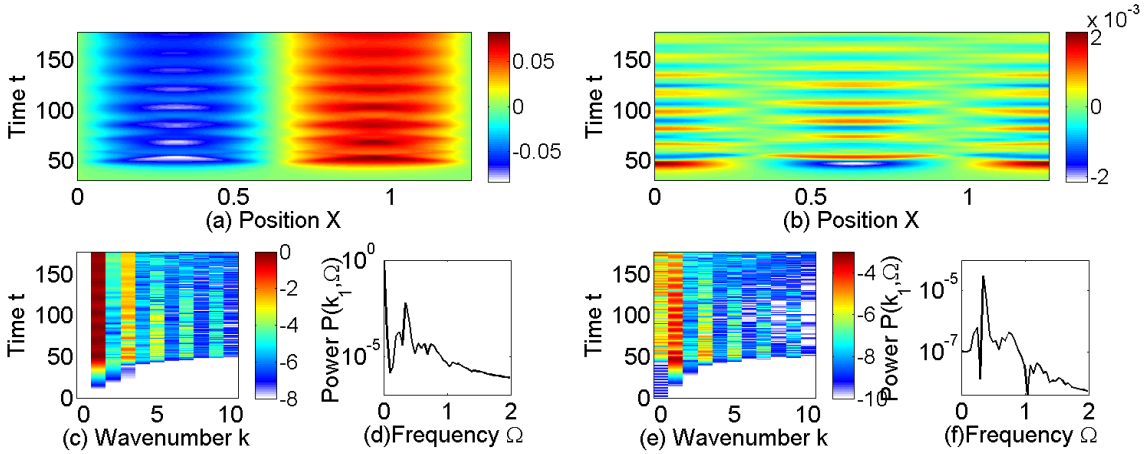

Figure 2. (Colour online) The electromagnetic fields: Panels (a) and (b) show B_y and E_z, respectively. Both are correlated and their phase difference is 90°. The E_z field is damped in time. Panel (c) shows the spatial power spectrum $log_{10}P(k,t)$ of B_y. The k_1 mode dominates, but harmonics can be seen. Panel (d) shows the frequency power spectrum $log_{10}P(k_1,\Omega)$ of B_y. Peaks are found at $\Omega = 0$ and $\Omega \approx 0.3$. Panel (e) evidences a $log_{10}P(k,t)$ of E_z resembling that of B_y in (c) and the $\log_{10} P(k_1,\Omega)$ of E_z in (f) also has a maximum at $\Omega \approx 0.3$. The power in (c,e) and (d,f) is normalized to the same value.

field components driven by the FI are investigated in Fig. 2. The B_y, E_z saturate at $t \approx 50$. The $B_y(x,t)$ then remains practically stationary, while $E_z(x,t)$ is damped.

We compute the spatial power spectrum $P(k,t)$ of B_y, E_z and E_x by a 1D Fourier transform over the full box length L and by taking the square of the amplitude modulus. The frequency power spectra (dispersion relation) are obtained through a 2D Fourier transform of the field data over the box length L and for $t > 50$. The amplitude moduli are then squared to give $P(k,\Omega)$. The base-10 logarithm of $P(k,t)$ of B_y in Fig. 2(c) evidences, that most power is concentrated in the mode k_1, with $k_s = 2\pi s/L$, and that the power in this mode is oscillating. Weaker harmonics with uneven s also occur. The $P(k_1,\Omega)$ of B_y reveals peaks at $\Omega = 0$ and $\Omega \approx 0.3$. The peak at $\Omega = 0$ dominates, because B_y is practically stationary after $t = 50$. The $P(k,t)$ and the $P(k_1,\Omega)$ of E_z in the Figs. 2(e,f) resemble qualitatively those of B_y, but they are weaker and the peak with $\Omega = 0$ is absent in the E_z-field.

The $E_x(x,t)$ in Fig. 3 reveals no spatial correlation with $B_y(x,t)$. The $P(k,t)$ of the E_x-field in Fig. 3(b) and of the B_y-field in Fig. 2(c) show no link between the k of the dominant waves. The spatial power spectrum $P(k,t)$ in Fig. 3(b) evidences instead a wave growth over a wide band of k. The E_x can not be driven by the QEI, because then the MPGF, which is $\partial_x \tilde{P}_{BY} = B_y dB_y/dx$ in our normalization, would imply that $E_x = 0$ whenever $B_y = 0$ or $dB_y/dx = 0$ and that it should oscillate in the k_2 mode. The $P(k,\Omega)$ of E_x in Fig. 3(c) reveals that the strongest waves have a $\Omega \approx 1$.

The particle phase space distributions provide more information. The electrons of the beam 1 (moves in positive z-direction) are species 1 and the positrons are species 3.

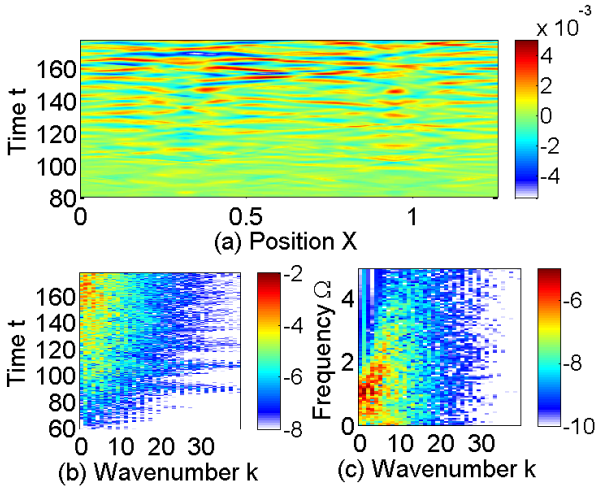

Figure 3. (Colour online) The electrostatic field: Panel (a) shows $E_x(x,t)$. Fluctuations grow at late times, which are distributed seemingly randomly in space. Its $\log_{10} P(k,t)$ in (b) evidences a broadband spectrum, that shows no dominant k. The $\log_{10} P(k,\Omega)$ peaks at $\Omega \approx 1$ and $k > 0$. The strongest fluctuations are propagating waves. The $P(k,t)$ and $P(k,\Omega)$ are normalized to the corresponding values of B_y.

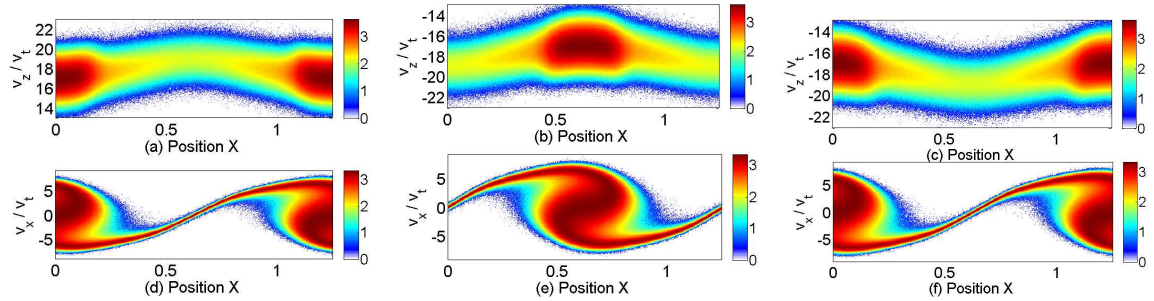

Figure 4. (Colour online) The base-10 logarithm of the phase space densities at the time $t = 50$ in units of CPs: Panels (a-c) display the $f(x, v_z)$ of the species 1, 2 and 4 (positrons). (d-f) show the $f(x, v_x)$ corresponding to the panels above them. The distributions in (d,f) are practically identical and (a,c) can be mapped onto each other by changing the sign of v_z. The $f(x, v_x)$ of species 1 and 2 are shifted by L/2.

The electrons and positrons of beam 2 are denoted as species 2 and 4, respectively. The current fluctuations of PIC simulations imply that $B_z, E_y \neq 0$. These fields correspond to waves that propagate in form of the high-frequency electromagnetic modes. However, the peak value of E_{EZ} exceeds the energy densities of E_y, B_z by 6 orders of magnitude and the latter remain practically constant during the simulation time. We can restrict our investigation to the phase space projections $f(x, v_x)$ and $f(x, v_z)$, because $B_x = 0$, $B_z \approx 0$ and $E_y \approx 0$. The $f(x, v_z)$ will reveal the electromagnetic structures, while the electrostatic structures are represented by $f(x, v_x)$. Figure 4 shows the phase space distributions of the species 1,2 and 4 at $t = 50$. The electrons of beam 1 and 2 are separated in space, which is typical of the FI driven by counter-streaming electron beams. The species 4 shows an $f(x, v_x)$ that is identical to that of species 1. The $f(x, v_z)$

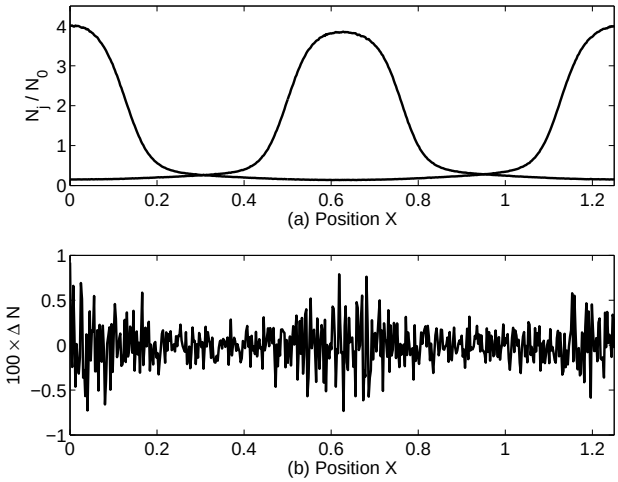

Figure 5. Panel (a) The number density distribution $N_j(x, t = 50)$ of the four species j in units of their mean density N_0. The curves $N_1(x)$ and $N_4(x)$ match (their differences amount to less than the thickness of the curves) and they peak at $x = 0$. The also matching $N_2(x)$ and $N_3(x)$ have their maximum at $x = L/2$. Panel (b) plots $\Delta N = \sum_j q_j N_j(x)/4N_0$, with $q_j = 1$ and -1 being the positron and electron charge. The fluctuations amount to less than 10^{-2} and they are by their scale size $\approx \Delta_x$ the statistical fluctuations due to the finite number of CPs per cell.

distribution of species 1 can be mapped onto that one of species 4 by switching the sign of v_z. Both these observations are expected, because in the absence of a significant E_x the opposite speed and charge of both species cancel. The Lorentz force thus displaces both species in the same way. The relation is also the same between the species 2 and 3. The high degree of symmetry is also demonstrated by the movie 1, which animates in time the projected phase space distributions of species 1, which is added to that of species 4. The color scale shows the base-10 logarithm of the number of CPs.

Figure 5 displays the number densities $N_i(x) = \int f_i(x, v_x) dv_x$ for each of the species i, normalized to the mean value $N_0 = \langle N_i(x) \rangle_x$. The $N_1 = N_4$ and $N_2 = N_3$ within the resolution of the image. The charge density modulations reach a peak value $\approx 4N_0$. This peak value is higher by a factor three and, accordingly, the filament confinement is thus stronger here than in Ref. [15], which did not consider positrons. Each species is represented by $N_p = 4.9 \times 10^4$ CPs per cell. The statistical fluctuations of the particle number are thus ${N_p}^{-0.5} \approx 5 \times 10^{-3}$, which is comparable to the measured charge density fluctuations $\Delta N = (4N_0)^{-1} \sum_i q_i N_i < 10^{-2}$ in Fig. 5(b). This observation, together with that the ΔN oscillates on a scale Δx, implies that the fluctuations at $t = 50$ are due to the finite number of CPs per cell. These fluctuations have a k-spectrum that is qualitatively similar to that of thermal noise. The fluctuation amplitude ΔN is increased within the filaments, e.g. in the interval $0.5 < x < 0.75$, because we have not normalized it to the local particle number, but to the average density.

Figure 6 displays the phase space distributions of the species 1, 2 and 4 at $t = 177$. The $f(x, v_z)$ are qualitatively unchanged compared to those in Fig. 4 and species 1 and 4 are still symmetric to a change of the sign of v_z. The distributions $f(x, v_x)$ reveal

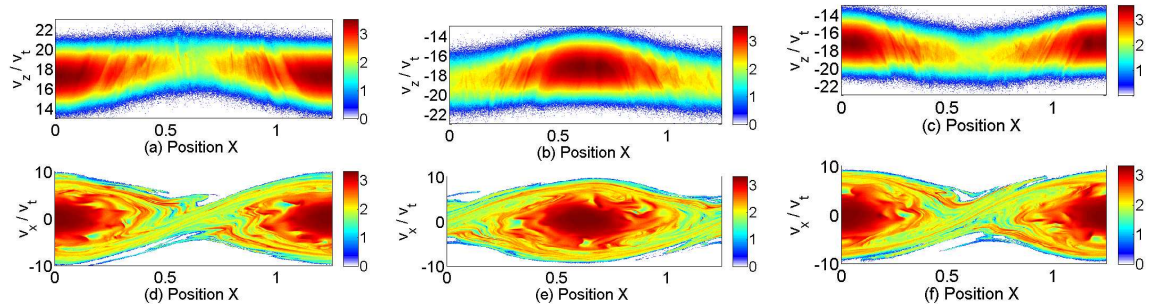

Figure 6. (Colour online) The base-10 logarithm of the phase space densities at the time $t = 177$ in units of CPs: Panels (a-c) show $f(x, v_z)$ of the species 1, 2 and 4, respectively. (d-f) show the $f(x, v_x)$ corresponding to the panels above. Species 1 and 4 reveal similar $f(x, v_x)$ and distributions $f(x, v_z)$ that are qualitatively symmetric to a change of the sign of v_z. The $f(x, v_x)$ of species 1 and 2 are shifted by L/2.

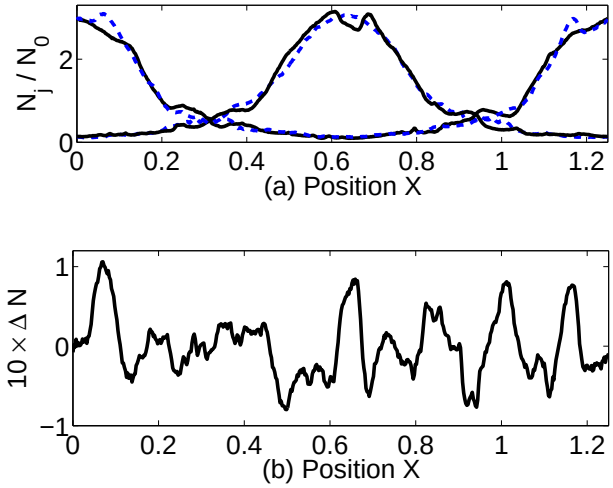

Figure 7. (Colour online) Panel (a) The $N_j(x)$ at the time t=177 of the four species j in units of N_0. The electron distributions $N_1(x)$ and $N_2(x)$ are denoted by the solid curves and N_3, N_4 are dashed and blue. The curves $N_1(x)$ and $N_4(x)$ peak at $x = 0$. The curves for electrons and positrons do not match. Panel (b) plots the $\Delta N = \sum_j q_j N_j(x)/4N_0$, with $q_j = 1$ and -1 being the positron and electron charge. The fluctuation amplitude is about 10 percent and they oscillate on scales $\gg \Delta x$.

that the particles are concentrated at the same positions as in Fig. 4. The particles have been heated up along the x-direction in between the dense filaments. The small scale structures, in particular in $f(x, v_x)$, differ for species 1 and 4 and we expect now clear charge density modulations. Figure 7 compares $N_1(x)$ with $N_4(x)$ and $N_2(x)$ with $N_3(x)$. Their differences can now be seen even from the N_i. The value $N_4(x = 0.08)$ exceeds that of $N_1(x = 0.08)$ by about 0.4 and fluctuations of this size occur in the entire box, which is demonstrated by the ΔN in Fig. 7(b). The typical length scale of the oscillations is about $0.1 \gg \Delta x$ and they are caused by the waves in Fig. 3.

The peak amplitude of E_x in Fig. 3 is $\approx 5 \times 10^{-3}$ at $t = 177$. The Lorentz force $v_b B_y$ for $v_b = 0.3$ and a maximum $B_y \approx 0.07$ at $t = 177$ (Fig. 2) is larger than

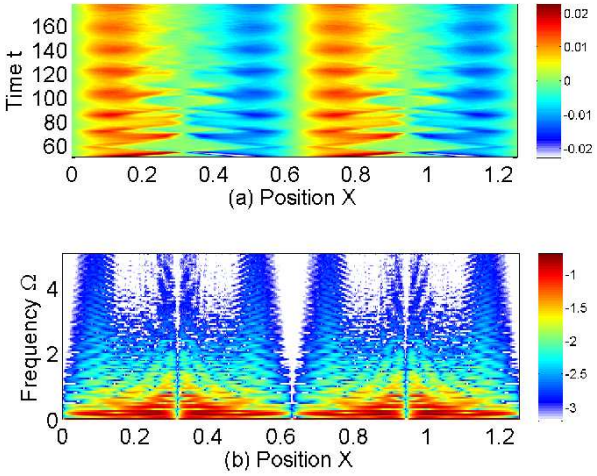

Figure 8. (Colour online) Panel (a) shows the magnetic pressure gradient force $B_y dB_y/dx$, which oscillates twice as fast in space as B_y. The MPGF is not stationary in time. Panel (b) displays the base-10 logarithm of the modulus of the spatial frequency spectrum $A(x, \Omega)$ of the MPGF. It is normalized to its peak value at $\Omega = 0$. Strong oscillations close to $x = L/4$ and $x = 3L/4$ reach $\Omega = 1$.

the electrostatic force by a factor of four. The electrostatic force is weaker before this time, while B_y is constant after $t = 50$. Thus, the electrons experience for most of the simulation duration the E_x only as a perturbation and the gyrofrequency of the CPs is determined by B_y and $v_z \approx v_b$, which is also demonstrated by the movie 1. The rotation of the dense filament in the distribution $f(x, v_x)$ has an approximately constant angular velocity in phase space. The structures in $f(x, v_z)$ and, thus, J_z will change with this characteristic frequency and impose the modulation of B_y and E_z with $\Omega \approx 0.3$ in the Fig. 2(d,f). This frequency is $\approx \Omega_i$, and consistent with the magnetic trapping.

The charge density fluctuations in Fig. 5(b) at $t = 50$ were at noise levels, which was expected from the low E_{EX} in Fig. 1 at this time and no QEI occured. It is only after the FI has saturated, that the electrostatic waves grow due to the SEI. The SEI yields the growth of E_{EX} in the interval $50 < t < 177$ and the waves in Fig. 3 have no obvious correlation with the B_y in Fig. 2. We will now identify one potential cause of the SEI. The force imposed by a magnetic pressure gradient on a current $\mathbf{J}$ is

$$\mathbf{J} \times \mathbf{B} = -\nabla \mathbf{B}^2/2. \tag{4}$$

Only B_y is growing in our 1D simulation box and the only possible spatial derivative is ∂_x. Equation 4 simplifies to $J_z B_y = B_y dB_y/dx$. The B_y is strong for $t > 50$ and $dB_y/dx \neq 0$. The MPGF on the right-hand side does, therefore, not vanish and the particles are accelerated.

Figure 8 shows the MPGF after $t = 50$ and $A(x, \Omega)$, which is its spatial frequency spectrum obtained by a Fourier transform over time. The maxima and minima of $\partial_x \tilde{P}_{BY}$ are stationary in space but its magnitude oscillates in time. The time average of the MPGF is positive to the right of the positions $x = 0$ and $x = L/2$ and negative to the

left of these positions. The $x = 0$ and $x = L/2$ coincide with the stable equilibrium points of the respective filaments. The MPGF is thus accelerating the particles away from the equilibrium points. The MPGF is, however, weaker than the drift force $q_j v_b B_y$, which is responsible for the filament confinement (magnetic trapping).

Consider the filament formed by the species 2 and 3 at $t = 50$, which is centred at $x = L/2$ in Fig. 5 and Fig. 8(a). The electrons of species 2 move with the velocity $\approx -v_b\mathbf{z}$, while the positrons of species 3 move with $\approx v_b\mathbf{z}$. Their currents have the same sign and the MPGF accelerates the electrons and the positrons into the same x-direction. As long as the positrons and the electrons have the same density everywhere, the E_x does not grow, because $J_x = 0$ in $\partial_t E_x + J_x = 0$. The term $\partial_y B_z - \partial_z B_y = 0$ in the 1D geometry. The MPGF does thus not result here in the E_x-field discussed in Ref. [13, 15], which has a wavelength that is half of that of the wave in B_y. However, the finite number of CPs introduces statistical fluctuations in the charge density (Fig. 5) that imply that the MPGF accelerates locally (on Debye length scales) a different number of electrons and positrons, by which $J_x \neq 0$. An electric field grows, that tries to restore the charge neutrality. The MPGF can couple to these fluctuations, if the force gradient is high (comparable to the spatial scale of the fluctuations) and if the force oscillates with the characteristic frequency of the fluctuations. Their dominant oscillation frequency in the spatial intervals with $B_y \approx 0$ is the plasma frequency and it is the upper-hybrid frequency otherwise. Figure 3(c) shows that the growing fluctuations have a broad frequency band and peak at $\Omega \approx 1$. The spatial gradients of the plasma density will, however, influence the fluctuation spectrum [37]. A force interacting with such fluctuations should thus also have a broad frequency band.

The spectrum $A(x, \Omega)$ in Fig. 8(b) reveals that the highest frequencies can be reached by the MPGF at $x \approx 0.1, 0.5, 0.7$ and at 1.1, although not with a high driving amplitude. The positions close to $x = L/4$ and $x = 3L/4$ experience stronger oscillations up to $\Omega = 1$. The MPGF changes also on spatial scales comparable to the Debye length, which is $v_t/c = 1/60$ in our normalization. An example is here a change at $t \approx 70$ and $x \approx 0.325$ in Fig. 8(a). The MPGF changes from 0.02 to -0.02 over a distance ≈ 0.03. The connection between the growth of E_{EX} and the oscillations of the MPGF is evidenced also by a comparison of Fig. 1 with Fig. 8(a). The growth of E_{EX} slows down at $t \approx 100$. The oscillations in Fig. 8(a) close to $L/4$ and $3L/4$ are more intense and shorter in duration before $t = 100$ and the spatial gradients are higher. The MPGF can thus couple easier energy to the charge density fluctuations. The spatio-temporal oscillations of $\partial_x \tilde{P}_{BY}$ soften up after $t = 100$, and the growth of E_{EX} slows down.

4. Discussion

In this paper we have considered the filamentation instability (FI) driven by two counterstreaming beams, each consisting of the electrons and positrons. The beams have initially been spatially uniform and the electromagnetic fields were set to zero. The 1D simulation is aligned with the x-direction, which excludes the merging of filaments

beyond a certain size and limits the physical realism of its nonlinear evolution [3]. However, the filaments are usually not circular but elongated [17, 18, 30]. A 1D geometry may thus be a valid approximation for those parts of filaments, which are quasi-planar such as the one investigated in Ref. [18]. The two beams move in opposite z-directions at the same speed modulus $v_b = 0.3$, which is sufficiently low to exclude significant relativistic effects. It is sufficiently high to obtain a linear growth rate of the FI that is comparable to those of the electrostatic modes and of the mixed modes. This may be further aided by the equal beam densities, which favor the filamentation instability if positrons are absent [22]. The strong electric fields with their oblique polarization in the PIC simulation in Ref. [28] demonstrate, however, that in particular the mixed modes would compete with the FI in a more realistic 2D or 3D simulation.

Our aim has been to obtain further insight into the dynamics of a filament pair formed by two counterpropagating beams of the electrons and positrons and to compare it with that of an electron filament pair. The simulation parameters are identical to those in the simulation in Ref. [15] that did not take into account the positrons. The short simulation box allows us to use a good statistical plasma representation and low noise levels. The charge density fluctuations inherent to the PIC simulation method provide noise over the full band of wavenumbers resolved by the simulation, out of which the wavemodes and any secondary instabilities can grow.

The FI redistributes the beams of charged particles in space into current filaments [3]. Our simulation box length L and the periodic boundary conditions allow only a single pair of filaments to grow. The centres of the electron filaments are spatially separated by the distance $L/2$ and this is also the case for both positron filaments. The filament formed by the electrons of one beam coincides with the filament containing the positrons of the second beam. Their phase space distributions $f(x, v_x)$, which hold the information about the electrostatic structures, match and their phase space distributions $f(x, v_z)$ can be mapped from one to the other by a change of the sign of v_z. The currents and densities of both components add up. The symmetry between the electrons and positrons within the same filament implies that the MPGF accelerates them into the same direction. We have found that their partial currents cancel each other until the FI saturates, implying that no E_x can grow due to the QEI.

The simulation in Ref. [15] evidenced that this E_x would accelerate the electrons away from the centre of the filament. The presence of the positrons in the simulation in the present work removes this repulsion. Higher charge and current densities can be reached by electron-positron beams compared to those containing only electrons and the spacing between the filaments is larger. The magnetic fields can reach higher spatial gradients. The magnetic fields grew to an amplitude set by magnetic trapping [11].

We have identified a SEI that is leading to a growing electrostatic energy density after the FI saturated, resulting in a broadband wave spectrum. The exponential growth rates of these waves remained well below that of the FI and they show no correlation with the MPGF. These observations are conflicting with the properties attributed to the QEI, implying that the SEI and the QEI must have different source mechanisms.

The finite number of computational particles imply statistical fluctuations of the charge density on Debye length scales. We have found here that the oscillation spectrum of the MPGF involves a wide band of frequencies that reach a maximum that exceeds the plasma frequency and that the MPGF changes significantly on scales comparable to the Debye length of the plasma after the FI has saturated. The MPGF can thus couple to the statistical fluctuations of the charge density. We have proposed that this coupling amplifies the fluctuations of J_x and E_x and that this is the cause of the SEI.

This hypothesis can be tested and the properties of the SEI can be examined in more detail with Vlasov simulations. They solve the Vlasov-Maxwell equations directly and do not approximate the plasma by phase space blocks. They are thus free of noise due to statistical plasma density fluctuations. The SEI should not develop in Vlasov simulations, unless seed fluctuations are introduced. The filaments, which are plasma structures resulting out of magnetic instabilities, would be more stable in Vlasov simulations than in PIC simulations. Previously, such an enhanced stability has only been reported for nonlinear structures (electron phase space holes) evolving out of purely electrostatic Buneman instabilities [38]. A localized charge density perturbation can be introduced into a Vlasov simulation and its interplay with the MPGF can be investigated. Such studies can not be performed with PIC codes, where we always have an ensemble of charge density perturbations interacting with the MPGF.

The energy density E_{EX} of the waves driven by the SEI remained below $10^{-2}E_{BY}$. The E_x-field will, however, not be negligible after $t = 177$, because the electric force $q_j E_x$ competes with the Lorentz force $q_j v_z B_y$ and $v_z < 1$. The ratio between the strongest Lorentz force and the strongest electric force has been 4 at $t = 177$ and the instability is growing. The SEI is also likely to play a more important role in PIC simulations that use only a low number of particles per cell. The higher relative charge density fluctuations imply, that the SEI grows from higher initial amplitudes, which reduces its growth time. The initial electric noise power scales approximately inversely proportional to the number of particles per cell. A reduction from our 4.9×10^4 particles per cell to 50 particles per cell will increase the initial power of E_x by the factor 10^3.

The energy density of the electric field has grown to a significant fraction of that of the magnetic field in the 1D and 2D simulations of counterpropagating electron beams [12, 13, 14, 15, 18], and it should influence the interplay of the filaments during their nonlinear evolution. No significant electric fields are observed during the quasi-linear growth phase of the FI and immediately after its saturation, if each beam carries electrons and positrons with an equal density. Our future studies will thus assess the impact of an absent electric field on the filament size distribution. This distribution can be approximated by a Gumbel distribution in 1D if no positrons are present [14]. We will also examine with 2D simulations how the filament size distribution orthogonal to the beam velocity vector evolves in time when positrons are present. The characteristic filaments size increases in the absence of the positrons linearly with time [17]. The impact of the electrostatic and mixed modes on the evolution of the filaments will also be addressed by 2D simulation studies that contain the beam velocity vector.

Acknowledgements The authors would like to thank the research councils of Sweden (Vetenskapsrådet) and Germany (DFG grant FOR1048) for financial support. The Swedish HPC2N computer centre has provided the computer time and support.

[1] Weibel E S 1959 *Phys. Rev. Lett.* **2** 83
[2] Morse R L and Nielson C W 1971 *Phys. Fluids* **14** 830
[3] Lee R and Lampe M 1973 *Phys. Rev. Lett.* **31** 1390
[4] Gremillet L, Benisti D, Lefebvre E and Bret A 2007, *Phys. Plasmas* **14** 040704
[5] Bret A, Firpo MC and Deutsch C 2005, *Phys. Rev. Lett.* **94**, 115002
[6] Bret A, Gremillet L, Benisti D and Lefebvre E 2008 *Phys. Rev. Lett.* **100** 205008
[7] Gallant YA and Arons J 1994 *Astrophys. J.* **435** 230
[8] Schlickeiser R and Shukla P K 2003 *Astrophys. J.* **599** L57
[9] Wilks S C, Kruer W L, Tabak M and Langdon A B 1992 *Phys. Rev. Lett.* **69** 1383
[10] Hill J M, Key M H, Hatchett S P, Freeman R R 2005 *Phys. Plasmas* **12** 082304
[11] Davidson R C, Hammer D A, Haber I and Wagner C E 1972 *Phys. Fluids* **15** 317
[12] Califano F, Pegoraro F, Bulanov S V and Mangeney A 1998 *Phys. Rev. E* **57** 7048
[13] Califano F, Cecchi T and Chiuderi C 2002 *Phys. Plasmas* **9** 451
[14] Rowlands G, Dieckmann M E and Shukla P K 2007 *New J. Phys.* **9** 247
[15] Dieckmann M E, Rowlands G, Kourakis I and Borghesi M 2008 *Plasma Phys. Controll. Fusion* submitted; arXiv:0810.5267
[16] Medvedev MV, Fiore M, Fonseca RA, Silva LO and Mori WB 2005 *Astrophys. J.* **618** L75
[17] Dieckmann M E, Lerche I, Shukla P K and Drury L O C 2007 *New J. Phys.* **9** 10
[18] Stockem A, Dieckmann M E and Schlickeiser R 2008 *Plasma Phys. Controll. Fusion* **50** 025002
[19] Sakai J I, Schlickeiser R and Shukla P K 2004 *Phys. Lett. A* **330** 384
[20] Bret A, Dieckmann M E and Deutsch C 2006 *Phys. Plasmas* **13** 082109
[21] Honda M, Meyer-ter-Vehn J and Pukhov A 2000 *Phys. Plasmas* **7** 1302
[22] Bret A, Gremillet L and Bellido J C 2007, *Plasma Phys. Controll. Fusion* **14** 032103
[23] Fiore M, Silva L O, Ren C, Tzoufras M A and Mori W B 2006 *Mon. Not. R. Astron. Soc.* **372** 1851
[24] Tautz R C and Sakai J I 2008 *J. Plasma Phys.* **74** 79
[25] Petri J and Kirk J G 2007 *Plasma Phys. Controll. Fusion* **49** 297
[26] Petri J and Kirk J G 2007 *Plasma Phys. Controll. Fusion* **49** 1885
[27] Tautz R C and Sakai J I 2008 *J. Plasma Phys.* **74** 815
[28] Kazimura Y, Sakai J I, Neubert T and Bulanov S V 1998 *Astrophys. J.* **498** L183
[29] Fonseca R A, Silva L O, Tonge J W, Mori W B and Dawson J M 2003 *Phys. Plasmas* **10** 1979
[30] Silva L O, 2006 *AIP Conf. Proc.* **856** 109
[31] Dawson J M 1983 *Rev. Mod. Phys.* **55** 403
[32] Eastwood J M 1991 *Comput. Phys. Commun.* **64** 252
[33] Godfrey B B 1974 *J. Comput. Phys.* **15** 504
[34] Langdon A B 1992 *Comput. Phys. Commun.* **70** 447
[35] Vallasenor J and Buneman O 1992 *Comput. Phys. Commun.* **69** 306
[36] Bowers K J, Albright B J, Yin L, Bergen B and Kwan T J T 2008 *Phys. Plasmas* **15** 055703
[37] Belyi V V 2002 *Phys. Rev. Lett.* **88** 255001
[38] Dieckmann M E, Eliasson B, Stathopoulos A and Ynnerman A 2004 *Phys. Rev. Lett.* **92** 065006